NANO · MICRO small
www.small-journal.com

Metal-Free Multi-Heteroatom-Doped Carbon Bifunctional Electrocatalysts Derived from a Covalent Triazine Polymer

Yong Zheng, Hui Song, Shan Chen, Xiaohui Yu, Jixin Zhu, Jingsan Xu, Kai A. I. Zhang, Chao Zhang,* and Tianxi Liu*

The construction of multi-heteroatom-doped metal-free carbon with a reversibly oxygen-involving electrocatalytic performance is highly desirable for rechargeable metal-air batteries. However, the conventional approach for doping heteroatoms into the carbon matrix remains a huge challenge owing to multistep postdoping procedures. Here, a self-templated carbonization strategy to prepare a nitrogen, phosphorus, and fluorine tri-doped carbon nanosphere (NPF-CNS) is developed, during which a heteroatom-enriched covalent triazine polymer serves as a "self-doping" precursor with C, N, P, and F elements simultaneously, avoiding the tedious and inefficient postdoping procedures. Introducing F enhances the electronic structure and surface wettability of the as-obtained catalyst, beneficial to improve the electrocatalytic performance. The optimized NPF-CNS catalyst exhibits a superb electrocatalytic oxygen reduction reaction (ORR) activity, long-term durability in pH-universal conditions as well as outstanding oxygen evolution reaction (OER) performance in an alkaline electrolyte. These superior ORR/OER bifunctional electrocatalytic activities are attributed to the predesigned heteroatom catalytic active sites and high specific surface areas of NPF-CNS. As a demonstration, a zinc-air battery using the NPF-CNS cathode displays a high peak power density of 144 mW cm^{-2} and great stability during 385 discharging/charging cycles, surpassing that of the commercial Pt/C catalyst.

1. Introduction

The ever-increasing energy demand promotes the vigorous exploitation of advanced and green energy techniques, such as rechargeable metal-air batteries, fuel cells, water electrolysis technologies, etc.[1–9] However, the sluggish kinetics of oxygen reduction reaction (ORR) and oxygen evolution reaction (OER) during discharge and charge processes has severely hampered their widespread applications.[10,11] Efficient electrocatalysts are required to accelerate ORR and OER. Although Pt and Ir/Ru-based catalysts were recognized as benchmark ORR and OER catalysts with superb intrinsic reaction activity, their widespread application has been impeded by their high price, poor durability, and single-functional electrocatalytic performance.[12] Therefore, the exploitation of inexpensive, efficient, and stable ORR/OER dual-functional electrocatalysts is an urgent need for clean energy technologies.

Heteroatom-doped carbon materials have been regarded as appealing

Y. Zheng, H. Song, S. Chen, X. Yu, Prof. C. Zhang, Prof. T. Liu
State Key Laboratory for Modification of Chemical Fibers and Polymer Materials
College of Materials Science and Engineering
Donghua University
Shanghai 201620, P. R. China
E-mail: czhang@dhu.edu.cn

Prof. J. Zhu
Shaanxi Institute of Flexible Electronics (SIFE)
Northwestern Polytechnical University (NPU)
127 West Youyi Road, Xi'an 710072, P. R. China

Prof. J. Xu
School of Chemistry
Physics and Mechanical Engineering
Queensland University of Technology
Brisbane, QLD 4001, Australia

Prof. K. A. I. Zhang
Department of Materials Science
Fudan University
Shanghai 200433, P. R. China
E-mail: kai_zhang@fudan.edu.cn

Prof. T. Liu
Key Laboratory of Synthetic and Biological Colloids
Ministry of Education
School of Chemical and Material Engineering
Jiangnan University
Wuxi 214122, P. R. China

Prof. T. Liu
Key Laboratory of Materials Processing and Mold (Zhengzhou University)
Ministry of Education
Zhengzhou 450002, P. R. China

The ORCID identification number(s) for the author(s) of this article can be found under https://doi.org/10.1002/smll.202004342.

DOI: 10.1002/smll.202004342

metal-free electrocatalysts owing to their competitive electrocatalytic activity, excellent conductivity, and facile preparation.[13–16] Nitrogen-doped carbons have been most widely researched because of their tunable electronic properties and great ORR electrocatalytic activities.[4] However, these carbon materials usually cannot be used as dual-functional electrocatalysts because of their poor OER activity.[17] Introducing P species into the carbon framework is a promising method to improve their OER electrocatalytic performance.[18–20] Nevertheless, the OER performance is not enhanced considerably due to their poor hydrophilicity and weak interaction with the electrolyte.[21,22] F atoms have the highest electronegativity, doping F can enhance the surface hydrophilicity of the catalyst, thus promoting the adsorption/desorption of ORR/OER electrocatalytic active intermediates.[23,24] Besides, fluorination of the neutral carbon skeleton can generate maximum charge polarization and defects for enhancing electrochemical activity and achieving excellent electrode stability.[25] Moreover, fluorination of the carbon matrix induces ionic C—F bond and semi-ionic C—F bond highly increased the adsorption of the oxygen molecule and activated O—O bond cleavage.[26] Lu and co-workers revealed that F-doping could markedly enhance the surface wettability of the as-made catalyst, thereby facilitating the mass transport and charge transfer in the porous carbon skeletons.[27] Panomsuwan et al. reported that ionic C—F bonds from F-doping can improve ORR activity.[28] Wang et al. revealed that F-doping can change the surface charge and increase the defects of the carbon matrix, leading to high electrocatalytic activity for OER.[29] Therefore, F-doping is particularly beneficial for improving the electrocatalytic performance of ORR and OER. Furthermore, multiple-heteroatom-doped carbon, especially N, P, F ternary species can synergistically generate a unique electronic structure and further improve the electrocatalytic activities. For instance, Dai's group discovered that N, P, and F codoped graphene showed excellent reaction activity for both HER, ORR, and OER.[30] Ma and co-workers found that N, P, F codoped carbon fibers showed great electrocatalytic behaviors toward ORR and OER.[31] However, most existing methods not only involve the inefficient multistep doping process but also simply mix different N, P, F sources with carbon precursors before thermal treatment. It generally caused surface functionalization without changing their bulk properties, which made it difficult to control the formation of uniformly distributed electrocatalytic active sites.[32] Compared to the conventional doping methods, using a single precursor to prepare N, P, F codoped carbon as metal-free ORR/OER dual-functional electrocatalysts is a promising synthetic strategy.

Recently, covalent triazine polymers (CTPs) have been considered as ideal precursors for preparing heteroatom-doped porous carbon due to their ultrahigh thermal stability, versatile elements incorporation, and large specific surface areas.[33,34] Additionally, different kinds of nonmetal dopants (e.g., N, B, F, P, S, etc.) in CTPs remain integrated into the carbon scaffolds, thus forming heteroatom electrocatalytic active sites.[35] It is, therefore, attractive to fabricate efficient metal-free electrocatalysts derived from heteroatom-enriched CTPs. In particular, due to the strong electrophilic effect of F atom, the CTP containing F element will possess ultrahigh thermal durability and thus greatly improve the doping efficiency.[36] However, the preparation of multi-heteroatom-doped carbon with heteroatom-enriched CTPs as a single precursor has never been reported yet.

Herein, we present an in situ one-step pyrolysis strategy to prepare an efficient ORR/OER bifunctional electrocatalyst, i.e., N, P, and F self-doped carbon spheres (NPF-CNS) derived from predesigned N, P, and F-enriched covalent triazine polymer (FP-CTP). Owing to the abundance and homogeneous distribution of N, P, and F in the FP-CTP framework, these heteroatoms were uniformly doped into the carbon skeletons to form efficient catalytic active centers. The as-made NPF-CNS-2 exhibited a superior ORR electrocatalytic performance in pH-universal condition from alkaline electrolyte (0.1 M KOH), acidic condition (0.5 M H_2SO_4 and 0.1 M $HClO_4$), to neutral media (0.1 M phosphate buffered saline (PBS)). Besides, the NPF-CNS-2 also showed great OER electrocatalytic activity and long-term durability in 1 M KOH electrolyte. Furthermore, the rechargeable zinc-air batteries assembled with NPF-CNS-2 as air electrodes demonstrate a small voltage gap (0.93 V), high maximum power density (144 mW cm^{-2}), and outstanding long-term stability (385 cycles).

2. Results and Discussion

The synthesis of the N, P, F self-doped carbon spheres is illustrated in **Scheme 1**. Initially, FP-CTP were rapidly synthesized by ultrasound-assisted precipitation polycondensation from N/P-enriched (HPPC) monomer and F-enriched (TFHQ) monomer. These were then carbonized under Ar atmosphere to acquire NPF-CNSs. Having a full crosslinked structure, FP-CTP as precursor prevented the loss of heteroatom ingredients during high-temperature carbonization. More importantly, using F-enriched TFHQ as monomer is favorable for improving the F-doping efficiency as well as obtaining uniform doping, which is usually impossible by traditional doping methods. Consequently, the resulted carbon exhibits great wettability that makes the electrolyte in close contact with the catalyst layer, thus leading to outstanding electrocatalytic performance for ORR and OER.

Scanning electron microscopy (SEM) images displayed that FP-CTP exhibited uniform spherical morphology (Figure S1, Supporting Information). Transmission electron microscopy (TEM) images showed the diameters of FP-CTP spheres were ≈660 nm (**Figure 1**a–c). These spheres were linked together to create a 3D crosslinked macroporous structure. By carefully screening different synthetic methods (ultrasonic, grinding, and solution stirring), reaction solvents (acetonitrile, tetrahydrofuran, ethyl acetate, and acetone), and reaction time (1, 10, 30, and 60 min), it was found that the optimized preparation method of FP-CTP was to use ultrasonic condition with acetonitrile as a solvent in 10 min (Figures S2–S4, Supporting Information). Besides, similar spherical morphologies were observed in the fluorine-free P-CTP sample (Figure S5, Supporting Information), suggesting the universality of this synthetic method. After pyrolysis at 900 °C under Ar atmosphere for 2 h, the spherical morphology is still well retained (Figure 1d,e and Figure S6c,d, Supporting Information). The well-maintained microstructure was probably attributed to the strong covalent

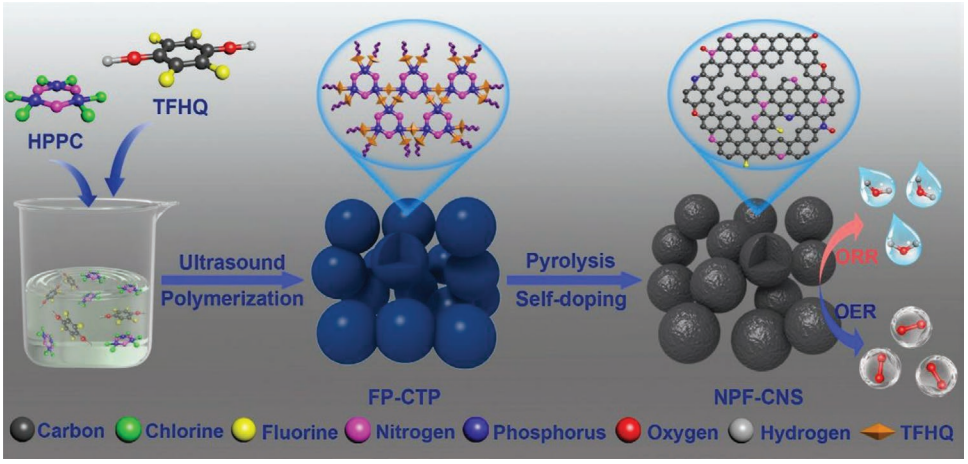

Scheme 1. Schematic illustration of the preparation procedure of NPF-CNSs.

bond interaction (e.g., C—F single bond) in the FP-CTP framework.[37] Notably, compared with the FP-CTP precursor, the optimal NPF-CNS-2 showed a smaller diameter (centered at 360 nm) and rougher surface, owing to weight loss during carbonization.[38] The high-resolution TEM (HRTEM) image manifested that NPF-CNS-2 has no obvious ordered carbon lattice fringes, suggesting that there are abundant defects and amorphous structures in NPF-CNS-2. Defects in the carbon matrix can modify the electronic structure, thus improving the ORR/OER activity.[39] Additionally, lots of white dots were observed in Figure 1f, demonstrating there are numerous micropores in the NPF-CNS-2. The existence of these micropores could be favorable for providing more accessible active sites, which further enhances the electrocatalytic activity.[40] The high-angle annular dark-field scanning transmission electron microscopy (HAADF-STEM) images and corresponding energy-dispersive spectrometer (EDS) mapping disclosed that the C, N, F, and P elements were homogeneously distributed in the carbon skeleton (Figure 1g), evidencing controllable doping of this method. The uniform heteroatom-doping could introduce heteroatom

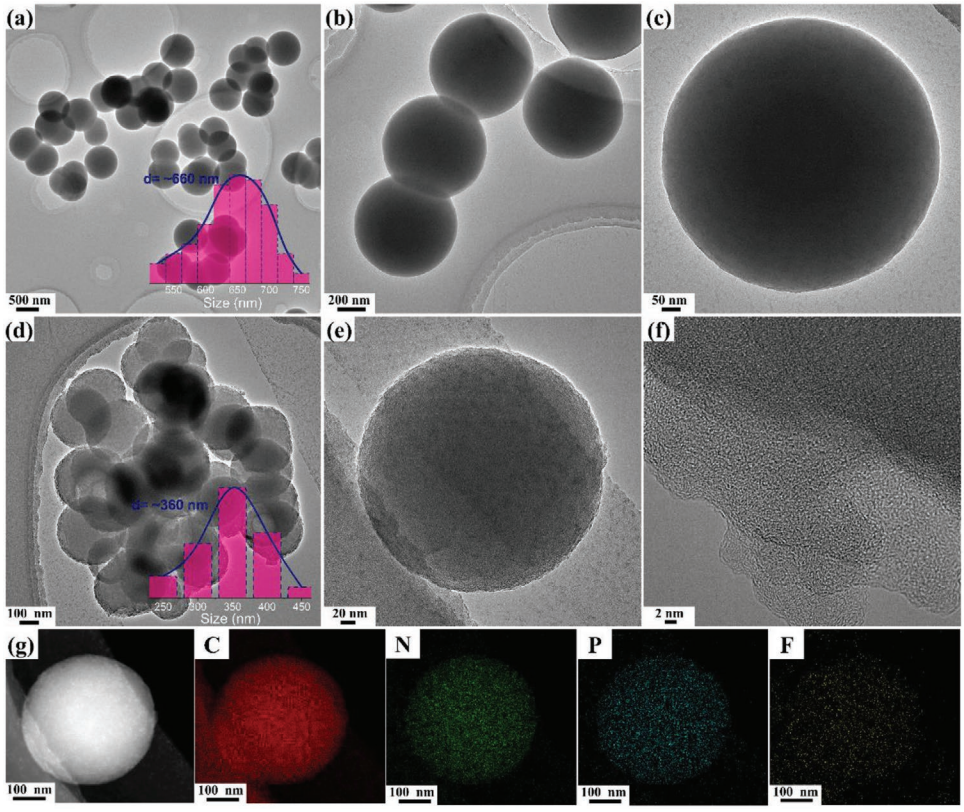

Figure 1. a–c) TEM images of FP-CTP. d,e) TEM and f) HRTEM images of NPF-CNS-2. g) STEM-EDS elemental mapping of NPF-CNS-2 for C, N, P, and F elements, respectively.

catalytic active centers and defects into carbon matrix, hence improve electrocatalytic activity.[20] Furthermore, the content of N, P, F in the carbon matrix was higher than other preparation methods,[29–31] suggesting this method is in favor of increasing the doping efficiency. Although the fact that NPF-CNS-1 well remained a spherical microstructure (Figure S6a,b, Supporting Information), it displayed poor links among each other and low graphitization degree, thus leading to poor conductivity compared with NPF-CNS-2 (Table S1, Supporting Information). While the spherical structures for the NPF-CNS-3 collapsed slightly (Figure S6e,f, Supporting Information), which may be owing to the excessive pyrolysis at over high temperature.

The successful polycondensation was demonstrated by Fourier transform infrared (FTIR) spectra and solid-state ^{13}P NMR spectra. The FTIR spectra of TFHQ and HQ in **Figure 2**a showed broad absorption peaks of the phenolic hydroxyl group (≈3294, 3184 cm^{-1}).[41] After the polycondensation, the above-mentioned absorption peaks disappeared, suggesting that the phenolic hydroxyl group of HQs has completely reacted with HCCP. A new absorption peak is located at 980 cm^{-1} for both FP-CTP and P-CTP, which is characteristic for P—O—(Ph).[42] Furthermore, the absorption of the corresponding phosphazene, C—F single bond, and phenyl absorptions were located at 1185, 1250, 1152, 1513, and 1465 cm^{-1}.[37] The existence of strong C—F covalent bonds led to the distinct decrease of electron cloud density and the increase of stability, thus greatly improved the carbonization yield and F-doping efficiency.[43] Besides, the obtained CTPs were characterized by ^{31}P CP/MAS NMR spectra. Figure 2b displays two resonance signals located at 3 and 19 ppm, suggesting the existence of —N=P[44]- and —N=P(—OPh)(—Cl)— structural units.[42] This result further demonstrated the successful polycondensation between HCCP and HQs. X-ray diffraction (XRD) pattern of CTPs showed two distinct diffraction patterns at about 11.2° and 22.3°, suggesting that CTPs possess certain ordering structures in the polymer framework (Figure 2c).[45] The thermal stability of CTPs was detected by thermogravimetric analysis (TGA). Figure 2d shows that FP-CTP has excellent thermal durability even at a high temperature of 521 °C, which was mainly due to the existence of a strong polar C—F single bond and clotriphosphazene rings in the fully crosslinked structures.[37] The weight retention of FP-CTP was more than 25 wt%, when even heated to 1000 °C under inert atmosphere, indicating that FP-CTP is a promising precursor to prepare versatile carbon materials on a large scale. Nitrogen sorption/desorption isotherms and corresponding pore size distribution curve affirmed coexistence of micropores and mesopores in the resulted CTPs (Figure S7, Supporting Information).[46]

Upon self-doped carbonization, the unique CTP precursor can be facilely converted into porous carbon spheres. Pyrolysis temperature played a crucial part in ORR/OER electrocatalytic activity by altering heteroatom contents, doped types as well as graphitization degrees. The XRD patterns of (002) and (100) crystalline planes for the NPF-CNSs are located at about 25.4° and 44.3°, respectively.[47] The intensity of corresponding peaks exhibited a gradual increase at elevated pyrolytic temperatures (Figure S8, Supporting Information), suggesting an enhanced graphitization degree.[48] More clearly, the diffraction pattern (002) located at about 25.4° becomes narrower and stronger at higher pyrolysis temperatures, suggesting that higher pyrolysis temperature promoted the formation of ordered graphitic carbon. Moreover, the (002) peak shifted from 25.4° in

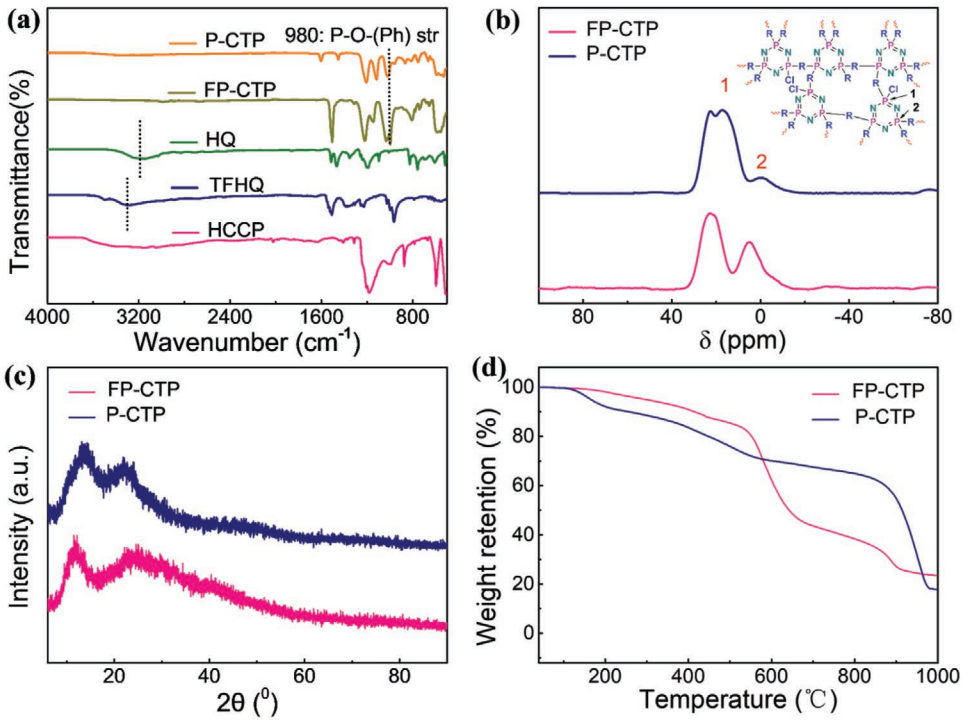

Figure 2. a) FTIR spectra of the monomers and corresponding CTPs. b) Solid-state ^{13}P NMR spectra, c) XRD patterns, and d) TGA curves of the FP-CTP and P-CTP.

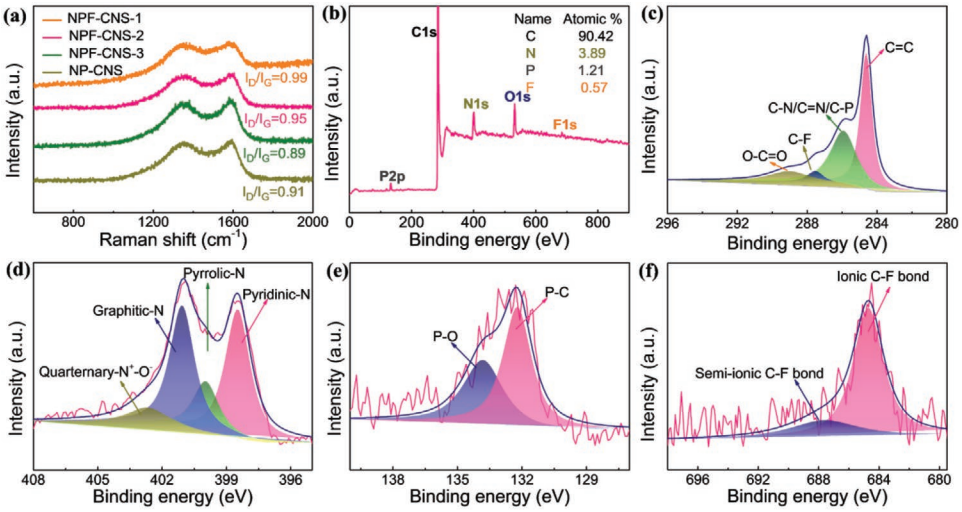

Figure 3. a) Raman spectra of the NPF-CNS-1, NPF-CNS-2, NPF-CNS-3, and NP-CNS. b) XPS survey spectra of the NPF-CNS-2. c–f) High-resolution C 1s, N 1s, P 2p, and F 1s XPS spectra of the NPF-CNS-2.

NP-CNS to 24.1° in NPF-CNS, indicating that the interlayer distance of NPF-CNS was enlarged due to the extra doping of F. After doping F, the interlayer distances increased from 0.352 to 0.364 nm calculated according to Bragg equation. **Figure 3**a depicts the Raman spectra of NPF-CNSs acquired under different annealing temperatures. They displayed two bands, namely, D bands (1336 cm^{-1}) and G bands (1580 cm^{-1}), which belonged to amorphous and graphitic carbon.[49] A smaller I_D/I_G value was obtained with pyrolysis temperature increasing from 800 to 1000 °C, manifested that preferable graphitization degree was formed under higher pyrolysis temperature. However, the total decrease of active sites with the increase of the pyrolytic temperature, which was demonstrated by X-ray photoelectron spectroscopy (XPS) characterizations (Table S2, Supporting Information). Thus, 900 °C is the optimum pyrolytic temperature, which is crucial to produce suitable active sites and conductivity. Besides, compared to NP-CNS, NPF-CNS-2 had an increased I_D/I_G value, indicating that F-doping induced more defects in NPF-CNS-2. These dopant-induced defects were considered as the major active sites and thus distinctly improving the electrocatalytic activity.[50]

The chemical information of NPF-CNSs was further investigated by XPS. As illuminated in Figure 3b, the survey XPS spectrum of NPF-CNS-2 showed obvious peaks for C, N, P, and F elements as expected. It had high F content (≈0.57 at%), P content (≈1.21 at%), and N content (≈3.89 at%), further proving that N, P, and F elements were efficiently doped into the carbon matrix (Table S2, Supporting Information). No fluorine signal was observed in the survey XPS spectrum of NP-CNS (Figure S9, Supporting Information). High-resolution C 1s spectrum of NPF-CNSs was divided into four distinct peaks 284.6, 285.9, 287.4, and 289.1 eV (Figure 3c and Figures S10a and 11a, Supporting Information), which were assigned to C=C, C—N/C—P, C—F, and O—C=O, respectively.[29] These results again demonstrated that the N, P, and F species were doped into the carbon skeleton successfully. Meanwhile, high-resolution N 1s spectrum (Figure 3d) could be divided into four peaks attributed to pyridinic-N (398.2 eV, 38.5 at%), pyrrolic-N (400.6 eV, 14.5 at%), graphitic-N (401.2 eV, 36.5 at%), and N→O (402.1 eV, 10.5 at%), respectively.[15] The higher proportions of graphitic-N as well as pyridinic-N in NPF-CNS-2 were significant because these two doped nitrogen species can largely improve the conductivity and electrocatalytic activity of the obtained catalysts.[4] High-resolution P 2p spectrum of NPF-CNS-2 was deconvoluted into two peaks, i.e., P—C (132.2 eV) and P—O (133.6 eV), indicating the formation of P-doped species (Figure 3e).[30] These groups are the main electrocatalytic active species by altering the charge distribution of the surrounding carbon atoms.[18–20] Figure 3f reveals that the high-resolution F 1s spectrum of NPF-CNS-2 exhibited ionic C—F bond (684.9 eV) and semi-ionic C—F bond (687. 8 eV). According to the literature, both of these bonds were associated with high ORR/OER electrocatalytic activity.[26,51–53] Moreover, the surface wettability of the catalysts before and after F-doping was investigated by contact angle measurements (Figure S12, Supporting Information). The measured contact angles of NP-CNS and NPF-CNS-2 are 70.1° and 27.9°, respectively. The contact angle decreases remarkably after F-doping, which was mainly attributed to the hydrophilic character of the polar ionic C—F bond in the doped carbon matrix.[23] The strong hydrophilicity of NPF-CNS-2 facilitates the transport of the ions/electron between the catalyst layer and electrolyte, which is beneficial to the corresponding electrocatalytic reaction.[54]

The N_2 adsorption/desorption profile of NPF-CNSs is revealed in Figure S13a (Supporting Information) to get insight into the surface area and porosity property of the CTPs-derived carbon materials. The corresponding pore size distribution curve (Figure S13b, Supporting Information) indicated that micropores are dominant in NPF-CNS-2, which agrees with the above TEM results. The Brunauer–Emmett–Teller (BET) surface areas and corresponding pore volumes for the CTPs and NPF-CNSs are summarized in Table S3 (Supporting Information). The results showed that the as-prepared catalyst from our synthesis strategy also features a high specific surface area with abundant porous structures. It was caused by the generated gases from the pyrolysis of CTPs via a self-activation

mechanism.[55] This further confirmed that heteroatom abundant CTPs can indeed be considered as ideal precursors for the preparation of metal-free carbon catalysts with abundant pores.[56] In this case, the predesigned N, P, F components in NPF-CNS-2 were fully exposed as active centers for improving ORR/OER electrocatalytic performance.

To investigate the electrocatalytic properties of NPF-CNSs, we initially evaluated its ORR performance in 0.1 M KOH using a rotating disk electrode technique. Cycle voltammetry (CV) measurements were tested to research the behaviors of NPF-CNSs and commercial Pt/C electrodes in N_2- and O_2-saturated electrolytes, respectively (**Figure 4**a). No typical redox peaks were observed from the CV curves in the N_2-saturated electrolyte. On the contrary, distinct reduction peaks arouse in O_2-saturated electrolyte, suggesting an intrinsic ORR electrocatalytic activity of NPF-CNSs. It can be observed that the oxygen reduction peak of NPF-CNS-2 is more positive than other catalysts, indicating that it is more effective for ORR. Additionally, linear scanning voltammetry curves were measured to further compare the electrocatalytic activities of all the as-obtained catalysts (Figure 4b). Among them, the optimal NPF-CNS-2 exhibits a superior ORR activity with higher onset potential (0.93 V) and half-wave potential (0.81 V) than those of NPF-CNS-1 and NPF-CNS-3, suggesting that a suitable annealing temperature is very important. Higher carbonization temperature will lead to a higher graphitization degree, which further improves the conductivity (Table S1, Supporting Information) and electrocatalytic activity.[57] In turn, over high carbonization temperature causes the collapse of the microstructure along with decomposition of the nitrogen, phosphorus, and fluorine heteroatom active sites (Table S2, Supporting Information). Meanwhile, NPF-CNS-2 also showed much higher half-wave potential than NP-CNS, confirming that F-doping can improve ORR catalytic activity. In comparison, the half-wave potential

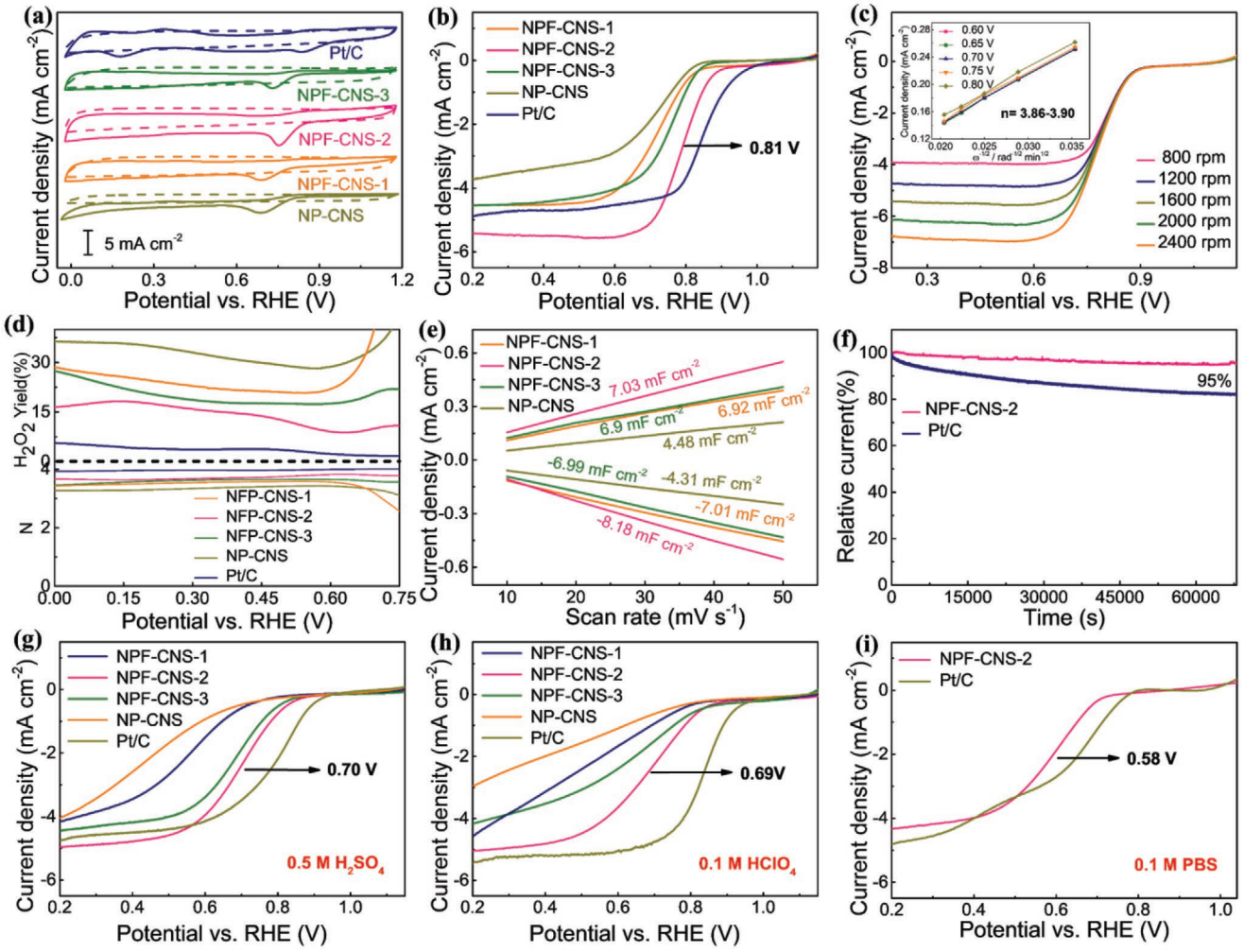

Figure 4. a) CV curves of NPF-CNS-1, NPF-CNS-2, NPF-CNS-3, NP-CNS, and Pt/C catalysts in N_2- and O_2-saturated 0.1 M KOH, respectively. b) LSV curves of NPF-CNS-1, NPF-CNS-2, NPF-CNS-3, NP-CNS, and Pt/C catalysts in O_2-saturated 0.1 M KOH, respectively. c) LSV curves of NPF-CNS-2 catalyst at various rotating speeds; Inset of (c) is K–L plots of NPF-CNS-2 catalyst at various potentials. d) Number of electrons transfer (n), and H_2O_2 yield plots for NPF-CNS-1, NPF-CNS-2, NPF-CNS-3, NP-CNS, and Pt/C catalysts calculated from the RRDE measurements. e) The measured capacitive currents plotted as a function of scan rates. f) Chronoamperometric responses of NPF-CNS-2 and Pt/C catalysts in O_2-saturated 0.1 M KOH, respectively. g, h) LSV curves of NPF-CNS-1, NPF-CNS-2, NPF-CNS-3, NP-CNS, and Pt/C catalysts in O_2-saturated 0.5 M H_2SO_4 and 0.1 M $HClO_4$, respectively. i) LSV curves of NPF-CNS-2 and Pt/C catalysts in O_2-saturated 0.1 M PBS, respectively.

of NPF-CNS-2 exhibited only ≈40 mV more negative than the Pt/C catalyst, which showed advantages over many reported metal-free electrocatalysts (Table S4, Supporting Information). What's more, the limiting current density of NPF-CNS-2 was larger than commercial Pt/C catalyst, owing to the introduction of rich heteroatom-doped catalytically active sites. The electron transfer number (N) was obtained based on LSV curves under various rotation rates (800–2400 rpm) and different potentials (0.60–0.80 V) by Koutecky–Levich (K–L) equation (Figure 4c). The corresponding K–L plots are presented in inset of Figure 4c, which exhibits a great linear relationship in potentials from 0.60 to 0.80 V. The calculated value of N was 3.86–3.90, confirming a perfect four-electron electrocatalytic reaction pathway.[29] While, NP-CNS sample with a lower N of 2.63–3.08, further demonstrated the unique doping effect of F atom for enhancing ORR performance (Figure S14, Supporting Information). Rotating ring-disk electrode (RRDE) measurement was further employed to study the ORR mechanism. As illustrated in Figure 4d, the average N value of NPF-CNS-2 was 3.85, which was very approach to commercial Pt/C catalyst (3.95) and superior to other catalysts. Besides, the H_2O_2 yield was less than 15%, revealed a high catalytic selectivity of NPF-CNS-2. To further study the intrinsic electrocatalytic activity of the resultant catalysts, electrochemical double-layer capacitance (C_{dl}) of them was examined by CV tests under different scan rates. As a result, NPF-CNS-2 showed the highest C_{dl} (11.32 mF cm^{-2}), which was much larger than NP-CNS (4.01 mF cm^{-2}), NPF-CNS-1 (6.98 mF cm^{-2}), and NPF-CNS-3 (8.51 mF cm^{-2}), confirmed the largest electrochemical active surface area (ECSA) of NPF-CNS-2 catalyst for ORR (Figure 4e and Figure S15, Supporting Information).[58]

In practical applications, long-term durability is another vital indicator of ORR electrocatalysts. Chronoamperometric assessments reflected that the NPF-CNS-2 exhibited high current retention (>95%) even after continuous test more than 70 000 s, whereas the commercial Pt/C catalyst showed only about 80% activity retention under the same condition (Figure 4f). Furthermore, a very small negative half-potential shift (10 mV) was showed after 10 000 CV cycles (Figure S16, Supporting Information). The good stability of NPF-CNS-2 is probably from the great durability of the intimately doped heteroatoms in carbon and the robustness of carbon skeleton.[48] The tolerance to methanol poisoning of the NPF-CNS-2 and commercial Pt/C catalysts was investigated (Figure S17, Supporting Information). Besides, for the NPF-CNS-2 catalyst, no remarkable current variations were noticed after adding 1 M methanol, whereas the Pt/C catalyst showed a distinct decrease of current. The robust structure of the carbon sphere network makes NPF-CNS-2 catalysts have good methanol poisoning tolerance. The above results demonstrated that NPF-CNS-2 is a metal-free electrocatalyst with great potential for ORR in practical applications.

The excellent ORR electrocatalytic activity of NPF-CNS-2 in alkaline electrolytes impelled us to study their electrocatalytic behaviors in acid and neutral conditions. Similar to the situation in alkaline media, NPF-CNS-2 also exhibited higher onset potentials and half-wave potentials than NPF-CNS-1, NPF-CNS-3, and NP-CNS in 0.1 M $HClO_4$ and 0.5 M H_2SO_4 electrolytes (Figure 4g,h). The above results confirmed that appropriate annealing temperature and F-doping were also very important in acidic electrolytes. Although the catalytic activity of NPF-CNS-2 was poorer than commercial Pt/C catalyst on half-wave and onset potentials, its limiting current density was very close to that of Pt/C. The activity still surpassed many reported metal-free ORR catalysts in acid conditions (Table S5, Supporting Information). The LSV curves of NPF-CNS-2 at different rotation speeds from 800 to 2400 rpm and corresponding K–L plots in Figure S19 (Supporting Information) (n = 3.70–3.97 at 0.20–0.60 V vs RHE), and RRDE measurement results in Figure S20 (Supporting Information) (average n = 3.87) both confirm a 4e$^-$ transfer pathway for NPF-CNS-2 in an acid electrolyte. Furthermore, the measured H_2O_2 yield was lower than 13% over the potential range from 0.20 to 0.80 V, disclosing the high O_2 reduction selectivity even in acidic conditions (Figure S20, Supporting Information). The C_{dl} of the as-prepared catalysts is probed by CV analysis (Figure S21, Supporting Information). The NPF-CNS-2 showed the highest C_{dl} (7.57 mF cm^{-2}), larger than other samples in 0.5 M H_2SO_4 (Figure S22, Supporting Information). The increase of ECSA resulted in the enhancement of the electrocatalytic activity of NPF-CNS-2. Moreover, NPF-CNS-2 also showed higher long-term durability and better methanol tolerance than the Pt/C catalyst in the acid electrolyte (Figures S23 and S24, Supporting Information). Searching for earth-abundant efficient metal-free catalysts to achieve high activities toward ORR under neutral conditions is highly desirable but still an urgent challenge. Remarkably, NPF-CNS-2 revealed a good ORR electrocatalytic activity close to Pt/C catalyst and great long-term stability in 0.1 M PBS buffer solution (Figure 4i and Figure S25, Supporting Information). The excellent ORR catalytic performance of NPF-CNS-2 over a wide range of pH can be attributed to the uniformly distributed N, P, F heteroatom active sites, great wettability, and high porosity in the robust carbon backbones. This is a rare example in metal-free ORR catalysts that the great electrocatalytic performance can be obtained at pH-universal conditions.

OER electrocatalytic activity plays a particularly important role in rechargeable zinc-air batteries. To further assess OER electrocatalytic performance, the activity of the as-made catalysts was tested in 1 M KOH medium. **Figure 5**a indicates that the NPF-CNS-2 showed an impressively low overpotential (340 mV) at a current density of 10 mA cm^{-2}, which was distinctly better than NPF-CNS-1 (400 mV), NPF-CNS-3 (365 mV), NP-CNS (380 mV), and approach to the advanced IrO_2 catalyst (330 mV). Moreover, the relatively low Tafel slope of 93 mV dec^{-1} is very close to that of the advanced IrO_2 catalyst of 84 mV dec^{-1} (Figure 5b and Figure S26, Supporting Information), revealing the favorable OER kinetics for NPF-CNS-2. The enhanced OER performance after F-doping was ascribed to the resulting high positive charge on carbon atoms, which could guarantee fast adsorption and exchange of O_2, OH^-, and H_2O species throughout the OER process.[52] The electrochemical impedance spectroscopy measurements confirmed that the charge-transfer resistance (R_{ct}) of NPF-CNS-2 was much smaller than the IrO_2 and other samples, indicated faster kinetics of the OER for NPF-CNS-2 (Figure S27, Supporting Information). A small catalytic degradation was observed in the chronoamperometry (i–t) curve for continuous test over 50 000 s, suggesting that NPF-CNS-2 had good OER long-term stability (Figure 5c). Furthermore, to further study the structural and chemical stability

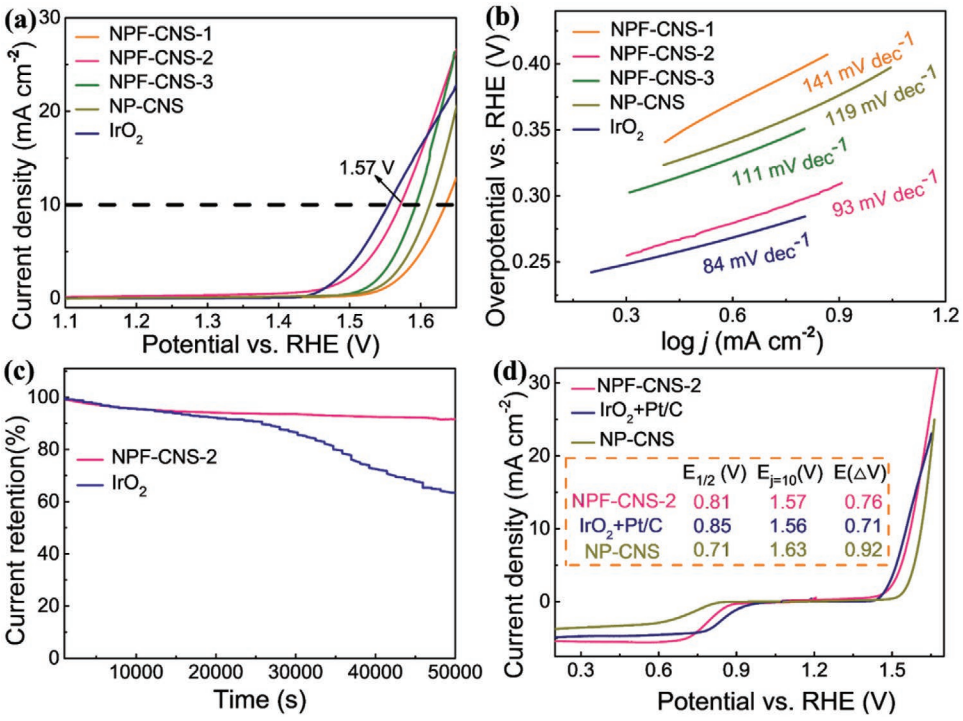

Figure 5. a) OER polarization curves of NPF-CNS-1, NPF-CNS-2, NPF-CNS-3, NP-CNS, and IrO_2 catalysts in 1 M KOH at a scan rate of 5 mV s^{-1} at 1600 rpm. b) Tafel plots of NPF-CNS-1, NPF-CNS-2, NPF-CNS-3, NP-CNS, and IrO_2 catalysts derived from OER polarization curves. c) Chronoamperometric responses of NPF-CNS-2 and IrO_2 catalysts in 1 M KOH, respectively. d) Comparison of the ΔE of various catalysts.

of the NPF-CNS-2 catalyst, we characterized and discussed the morphology and composition of the as-prepared catalyst after the stability test. SEM and TEM observation revealed the microstructure of NPF-CNS-2 is unchanged after the stability test (as shown in Figure S28a–c, Supporting Information). Also, corresponding elemental mapping images (Figure S28d, Supporting Information) reveal that numerous N, P, and F elements still exist and homogeneously distribute in the carbon matrix, demonstrating that the as-made material has good structural stability. According to Raman spectra (Figure S29a, Supporting Information), after the stability test, the ratio of the relative intensity between D band and G band slightly increased to 0.98, which was mainly attributed to the slight corrosion of the carbon skeleton during the long testing process. This result further indicated the carbon matrix has good chemical stability. After the stability test, the XPS spectrum of NPF-CNS-2 showed the intensity of the O 1s peak increased (Figure S29b, Supporting Information). More specifically, the relative intensities of O–C = O, P–O and Quarternary–N^+–O^- increase slightly (Figure S29c–e, Supporting Information), which could be ascribed to the slight oxidation of the carbon matrix. To explore the influence of OER testing on ORR catalytic activity, the LSV curve of NPF-CNS-2 after the OER test is shown in Figure S30 (Supporting Information), in which the half-wave potential has only a minimal negative shift of 11 mV.

The bifunctional electrocatalytic performance of the catalysts can be evaluated by the potential difference (ΔE) between half-wave potential ($E_{1/2}$) for ORR and current density at 10 mA cm^{-2} ($E_{j\,=\,10}$) for OER. Figure 5d shows that NPF-CNS-2 had a small ΔE value (0.76 V), which was much better than the NP-CNS (0.92 V) and close to the mixture of commercial Pt/C and IrO_2 catalyst (0.71 V). Enough catalytically active sites and remarkable hydrophilic property caused by a multi-heteroatom-doped effect synergistically heightens the superior reversible oxygen electrocatalytic performance of NPF-CNS-2 catalyst. More specifically, 1) the electron-withdrawing groups (e.g., pyridinic N and C=O) within the carbon matrix can make the adjacent carbon atoms positively charged, which could then facilitate the adsorption of the ORR and OER intermediates;[59] 2) P atoms can polarize the adjacent carbon atoms and induce defects, resulting in a catalytic site to the ORR/OER;[60] 3) doping F can enhance the surface hydrophilicity of the catalyst, thus promoting the adsorption/desorption of ORR/OER electrocatalytic active species.[23] **Tables 1** and **2** summarize electrocatalytic properties for the as-designed catalysts at various pH values. Besides, the ORR/OER bifunctional performance of the NPF-CNS-2 catalyst ranked at the top level among the variously reported electrocatalysts (Table S6, Supporting Information).

In consideration of its outstanding ORR and OER performance of the NPF-CNS-2, we then assembled a rechargeable zinc-air battery to assess the practical application in cathode materials. The catalyst was coated onto a carbon paper and contacted stainless steel as air cathode, a copper foil contacted zinc plate was used as metal anode, and an aqueous KOH (6 M) solution containing 0.2 M $Zn(OAc)_2$ as electrolyte (Figure S31, Supporting Information). **Figure 6**a shows a schematic of the rechargeable zinc-air battery. Figure S32 (Supporting Information) indicates that the NPF-CNS-2-based battery works more smoothly with the similar open-circuit potential of Pt catalyst (1.49 V). Moreover, a light-emitting-diode (LED) lamp was lit

Table 1. ORR performance of NP-CNS, NPF-CNS-1, NPF-CNS-2, and NPF-CNS-3 catalysts in electrolytes at various pH values.

Sample	E_{onset} (V vs RHE)	$E_{1/2}$ (V vs RHE)	J_L [mA cm^{-2}]	Electrolyte
NP-CNS	0.82	0.69	3.73	0.1 M KOH
	0.78	0.60	4.01	0.1 M $HClO_4$
	0.70	0.48	2.98	0.5 M H_2SO_4
NPF-CNS-1	0.83	0.65	4.51	0.1 M KOH
	0.79	0.56	4.12	0.1 M $HClO_4$
	0.72	0.58	4.52	0.5 M H_2SO_4
NPF-CNS-2	0.90	0.81	5.42	0.1 M KOH
	0.82	0.69	5.01	0.1 M $HClO_4$
	0.83	0.70	5.03	0.5 M H_2SO_4
	0.70	0.58	4.23	0.1 M PBS
NPF-CNS-3	0.85	0.72	4.51	0.1 M KOH
	0.81	0.62	4.42	0.1 M $HClO_4$
	0.80	0.68	4.18	0.5 M H_2SO_4

up easily by two series-assembled zinc-air batteries or over 10 h without the brightness fading (Figure 6b). Noticeably, from the polarization curve (Figure 6c), the NPF-CNS-2 electrode showed a high-power density (144 mW cm^{-2}), which exceeded the commercial Pt/C catalyst (112 mW cm^{-2}). Figure 6d shows that the voltage gap of NPF-CNS-2 was distinctly smaller than commercial Pt/C during charging and discharging processes, suggesting a more efficient rechargeability. Furthermore, the voltage platform of NPF-CNS-2 at different current densities was higher than the commercial Pt/C catalyst, which coincided well with the good durability in the ORR assessment (Figure 6e). The superior rate performance is due to the facilitated active species transport from the porous structure of NPF-CNS-2 in large discharge currents. Figure 6f displays the charge/discharge stability of the air cathodes of the NPF-CNS-2 and simple mixture of commercial Pt/C and IrO_2 (Pt/C + IrO_2) at a constant current density of 5 mA cm^{-2}. The NPF-CNS-2 air-electrode revealed outstanding cycling stability for 125 h without no obvious voltage changes over 385 charge/discharge cycles, while the Pt/C + IrO_2 catalysts showed an increased overpotential in charge and discharge process when up to 295 cycles.

3. Conclusions

In summary, a self-templated carbonization strategy was developed for fabricating a porous N, P, and F codoped carbon catalyst. The integration of N, P, and F elements into the CTP precursor is beneficial for the one-pot self-doping of the NPF-CNS with uniformly distributed heteroatom active sites. As a result, the optimal NPF-CNS-2 exhibited high electrocatalytic activity, outstanding long-term durability for the ORR under universal pH environments. Also, NPF-CNS-2 is capable of being employed as an efficient OER catalyst, and the calculated ΔE (namely, $E_{j\ =\ 10} - E_{1/2}$) value is only 0.76 V, beyond most of the reported metal-free catalysts. Moreover, the rechargeable zinc-air batteries using the NPF-CNS-2 as the cathode presented superior charge–discharge stability (385 cycles), remarkably outperforming commercial Pt/C catalyst (295 cycles). Our study offers a new design strategy for preparing multi-heteroatom-doped and metal-free carbon electrocatalysts for high power electrochemical energy conversion devices.

Table 2. OER performance of NP-CNS, NPF-CNS-1, NPF-CNS-2, and NPF-CNS-3 catalysts in 1 M KOH electrolyte.

Sample	η at 10 mA cm^{-2}	Tafel [mV dec^{-1}]
NP-CNS	1.62	119
NPF-CNS-1	1.64	141
NPF-CNS-2	1.57	93
NPF-CNS-3	1.59	111

4. Experimental Section

Preparation of CTP: The FP-CTP was prepared by an ultrasonic-assisted polycondensation. In brief, HCCP (0.4 g) and TFHQ (0.63 g) were added to a 250 mL beaker, followed by the addition of CH_3CN (100 mL) to form a uniform solution, and then TEA (1.0 mL) was injected to the above solution. The molar ratio of TFHQ to HCCP was 3:1 (by stoichiometry). The solution was kept under ultrasonic condition (200 W, 70 kHz) at room temperature for 10 min. After that, the produced white solids were washed three times by CH_3CN, DMF, ethanol, and deionized water, respectively. The resulting white powders were dried under vacuum at 60 °C overnight to obtain the FP-CTP. For comparison, other precursors were prepared via a similar process with fluorine-free HQ monomer, which was denoted as P-CTP. Besides, different solvents, reaction time, and preparation methods were screened to obtain the comparison samples.

Preparation of NPF-CNS: Typically, FP-CTP powders were subjected to carbonization at 800, 900, and 1000 °C for 2 h under Ar atmosphere at an invariable heating rate (5 °C min^{-1}). Upon cooling down naturally to RT, the as-obtained samples were washed with deionized water to remove inactive and unstable substances. Finally, the products were denoted as NPF-CNS-*X*, where *X* represents the pyrolytic temperatures. Namely,

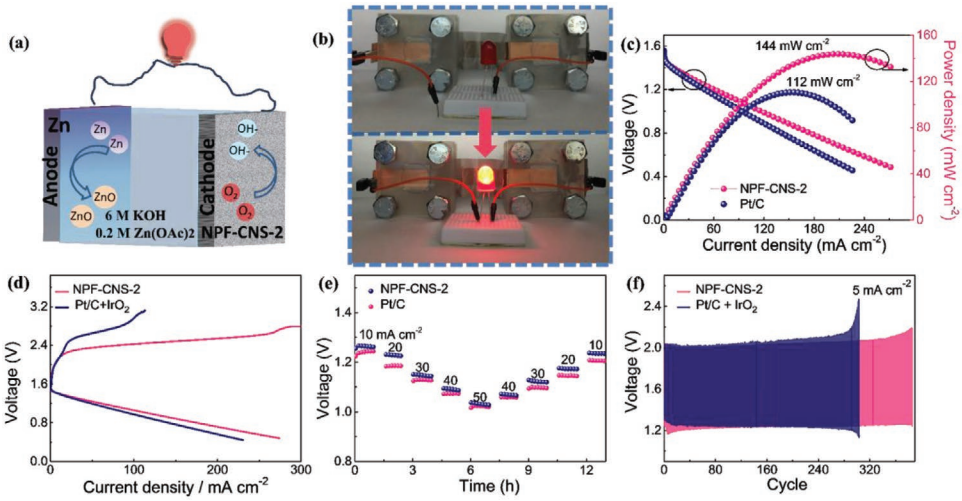

Figure 6. a) Schematic illustration of the zinc-air battery. b) Photographs showing an LED light powered by two as-assembled zinc-air batteries in series. c) Discharge polarization curves and power density curves of zinc-air batteries using NPF-CNS-2 and commercial Pt/C cathodes. d) Charge and discharge curves of rechargeable zinc-air batteries using NPF-CNS-2 and commercial Pt/C+IrO_2 cathodes. e) Rate performance of NPF-CNS-2 and Pt/C electrodes at a current density of 10, 20, 30, 40, 50, and 10 mA cm^{-2}, respectively. f) Galvanostatic charge and discharge cycling curves of rechargeable zinc-air batteries with NPF-CNS-2 and commercial Pt/C+IrO_2 cathodes at a current density of 5 mA cm^{-2}.

NPF-CNS-1, NPF-CNS-2, and NPF-CNS-3 mean the products pyrolyzed at 800, 900, and 1000 °C, respectively. As a convenient comparison, another catalyst was also pyrolyzed at 900 °C via the similar procedures with P-CTP as the precursor, named as NP-CNS.

Supporting Information

Supporting Information is available from the Wiley Online Library or from the author.

Acknowledgements

The authors are grateful for the financial support from the National Natural Science Foundation of China (51773035), the Shanghai Rising-Star Program (18QA1400200), and the Shanghai Scientific and Technological Innovation Project (18JC1410600).

Conflict of Interest

The authors declare no conflict of interest.

Keywords

heteroatom active sites, metal-free electrocatalysts, N, P, F self-doping, oxygen evolution reaction, oxygen reduction reaction

Received: July 18, 2020
Revised: September 15, 2020
Published online:

[1] R. Cao, J.-S. Lee, M. Liu, J. Cho, *Adv. Energy Mater.* **2012**, *2*, 816.
[2] Y. Li, H. Dai, *Chem. Soc. Rev.* **2014**, *43*, 5257.
[3] H. B. Yang, J. Miao, S.-F. Hung, J. Chen, H. B. Tao, X. Wang, L. Zhang, R. Chen, J. Gao, H. M. Chen, L. Dai, B. Liu, *Sci. Adv.* **2016**, *2*, e1501122.
[4] K. Gong, F. Du, Z. Xia, M. Durstock, L. Dai, *Science* **2009**, *323*, 760.
[5] C. Zhang, M. Antonietti, T.-P. Fellinger, *Adv. Funct. Mater.* **2014**, *24*, 7655.
[6] L. Han, S. Song, M. Liu, S. Yao, Z. Liang, H. Cheng, Z. Ren, W. Liu, R. Lin, G. Qi, X. Liu, Q. Wu, J. Luo, H. L. Xin, *J. Am. Chem. Soc.* **2020**, *142*, 12563.
[7] F. Lv, N. Han, Y. Qiu, X. Liu, J. Luo, Y. Li, *Coord. Chem. Rev.* **2020**, *422*, 213435.
[8] Y. Mi, Y. Qiu, Y. Liu, X. Peng, M. Hu, S. Zhao, H. Cao, L. Zhuo, H. Li, J. Ren, X. Liu, J. Luo, *Adv. Funct. Mater.* **2020**, *30*, 2003438.
[9] S. Shen, X. Peng, L. Song, Y. Qiu, C. Li, L. Zhuo, J. He, J. Ren, X. Liu, J. Luo, *Small* **2019**, *15*, 1902229.
[10] A. A. Gewirth, J. A. Varnell, A. M. DiAscro, *Chem. Rev.* **2018**, *118*, 2313.
[11] Z.-F. Huang, J. Wang, Y. Peng, C.-Y. Jung, A. Fisher, X. Wang, *Adv. Energy Mater.* **2017**, *7*, 1700544.
[12] Z. Wang, Y. Lu, Y. Yan, T. Y. P. Larissa, X. Zhang, D. Wuu, H. Zhang, Y. Yang, X. Wang, *Nano Energy* **2016**, *30*, 368.
[13] T. Zhu, Q. Feng, S. Liu, C. Zhang, *Compos. Commun.* **2020**, *20*, 100376.
[14] I.-Y. Jeon, S. Zhang, L. Zhang, H.-J. Choi, J.-M. Seo, Z. Xia, L. Dai, J.-B. Baek, *Adv. Mater.* **2013**, *25*, 6138.
[15] S. Yang, L. Zhi, K. Tang, X. Feng, J. Maier, K. Müllen, *Adv. Funct. Mater.* **2012**, *22*, 3634.
[16] L. Li, Y. Zhang, H. Lu, Y. Wang, J. Xu, J. Zhu, C. Zhang, T. Liu, *Nat. Commun.* **2020**, *11*, 62.
[17] Y. Jiao, Y. Zheng, M. Jaroniec, S. Z. Qiao, *J. Am. Chem. Soc.* **2014**, *136*, 4394.
[18] T. Najam, S. S. A. Shah, W. Ding, J. Jiang, L. Jia, W. Yao, L. Li, Z. Wei, *Angew. Chem., Int. Ed.* **2018**, *57*, 15101.
[19] Z. Liu, J. Ai, M. Sun, F. Han, Z. Li, Q. Peng, Q.-D. Wang, J. Liu, L. Liu, *Adv. Funct. Mater.* **2020**, *30*, 1910741.
[20] J. Zhang, Z. Zhao, Z. Xia, L. Dai, *Nat. Nanotechnol.* **2015**, *10*, 444.
[21] J. P. Paraknowitsch, A. Thomas, *Energy Environ. Sci.* **2013**, *6*, 2839.
[22] T. Y. Ma, J. Ran, S. Dai, M. Jaroniec, S. Z. Qiao, *Angew. Chem., Int. Ed.* **2015**, *54*, 4646.

[23] X. Sun, Y. Zhang, P. Song, J. Pan, L. Zhuang, W. Xu, W. Xing, *ACS Catal.* **2013**, *3*, 1726.
[24] W. He, Y. Wang, C. Jiang, L. Lu, *Chem. Soc. Rev.* **2016**, *45*, 2396.
[25] X. Qiao, S. Liao, G. Wang, R. Zheng, H. Song, X. Li, *Carbon* **2016**, *99*, 272.
[26] X. Sun, P. Song, Y. Zhang, C. Liu, W. Xu, W. Xing, *Sci. Rep.* **2013**, *3*, 2505.
[27] H. Zhou, Y. Peng, H. B. Wu, F. Sun, H. Yu, F. Liu, Q. Xu, Y. Lu, *Nano Energy* **2016**, *21*, 80.
[28] G. Panomsuwan, N. Saito, T. Ishizaki, *J. Mater. Chem. A* **2015**, *3*, 9972.
[29] L. Wang, Y. Wang, M. Wu, Z. Wei, C. Cui, M. Mao, J. Zhang, X. Han, Q. Liu, J. Ma, *Small* **2018**, *14*, 1800737.
[30] J. Zhang, L. Dai, *Angew. Chem., Int. Ed.* **2016**, *128*, 13490.
[31] M. Wu, Y. Wang, Z. Wei, L. Wang, M. Zhuo, J. Zhang, X. Han, J. Ma, *J. Mater. Chem. A* **2018**, *6*, 10918.
[32] L. Zhao, X.-L. Sui, J.-Z. Li, J.-J. Zhang, L.-M. Zhang, G.-S. Huang, Z.-B. Wang, *Appl. Catal., B* **2018**, *231*, 224.
[33] Y. Li, S. Zheng, X. Liu, P. Li, L. Sun, R. Yang, S. Wang, Z.-S. Wu, X. Bao, W.-Q. Deng, *Angew. Chem., Int. Ed.* **2018**, *57*, 7992.
[34] L. Hao, S. Zhang, R. Liu, J. Ning, G. Zhang, L. Zhi, *Adv. Mater.* **2015**, *27*, 3189.
[35] E. Gottlieb, K. Matyjaszewski, T. Kowalewski, *Adv. Mater.* **2019**, *31*, 1804626.
[36] X.-H. Xu, K. Matsuzaki, N. Shibata, *Chem. Rev.* **2015**, *115*, 731.
[37] A. X. Wu, J. A. Drayton, K. M. Rodriguez, Q. Qian, S. Lin, Z. P. Smith, *Macromolecules* **2020**, *53*, 5085.
[38] D. S. Bin, Z. X. Chi, Y. T. Li, K. Zhang, X. Z. Yang, Y. G. Sun, J. Y. Piao, A. M. Cao, L. J. Wan, *J. Am. Chem. Soc.* **2017**, *139*, 13492.
[39] C. Tang, Q. Zhang, *Adv. Mater.* **2017**, *29*, 1604103.
[40] F.-L. Meng, Z.-L. Wang, H.-X. Zhong, J. Wang, J.-M. Yan, X.-B. Zhang, *Adv. Mater.* **2016**, *28*, 7948.
[41] Y. Zheng, F.-L. Qing, Y. Huang, X.-H. Xu, *Adv. Synth. Catal.* **2016**, *358*, 3477.
[42] L. Zhu, Y. Zhu, Y. Pan, Y. Huang, X. Huang, X. Tang, *Macromol. React. Eng.* **2007**, *1*, 45.
[43] T. Zhu, S. Liu, K. Wan, C. Zhang, Y. Feng, W. Feng, T. Liu, *ACS Appl. Energy Mater.* **2020**, *3*, 4949.
[44] H. Wang, H.-W. Lee, Y. Deng, Z. Lu, P.-C. Hsu, Y. Liu, D. Lin, Y. Cui, *Nat. Commun.* **2015**, *6*, 7261.
[45] X. Wang, C. Zhang, Y. Zhao, S. Ren, J.-X. Jiang, *Macromol. Rapid Commun.* **2016**, *37*, 323.
[46] F. Lai, C. Yang, R. Lian, K. Chu, J. Qin, W. Zong, D. Rao, J. Hofkens, X. Lu, T. Liu, *Adv. Mater.* **2020**, 2002474.
[47] K. Tang, L. Fu, R. J. White, L. Yu, M.-M. Titirici, M. Antonietti, J. Maier, *Adv. Energy Mater.* **2012**, *2*, 873.
[48] Z. Pei, H. Li, Y. Huang, Q. Xue, Y. Huang, M. Zhu, Z. Wang, C. Zhi, *Energy Environ. Sci.* **2017**, *10*, 742.
[49] J. Du, L. Liu, Z. Hu, Y. Yu, Y. Qin, A. Chen, *Adv. Funct. Mater.* **2018**, *28*, 1802332.
[50] X. Yan, Y. Jia, X. Yao, *Chem. Soc. Rev.* **2018**, *47*, 7628.
[51] S. Akula, A. K. Sahu, *J. Electrochem. Soc.* **2019**, *166*, F93.
[52] J. Kim, R. Zhou, K. Murakoshi, S. Yasuda, *RSC Adv.* **2018**, *8*, 14152.
[53] L. Cao, X. Zhou, Z. Li, K. Su, B. Cheng, *J. Power Sources* **2019**, *413*, 376.
[54] S. Gao, Y. Chen, H. Fan, X. Wei, C. Hu, H. Luo, L. Qu, *J. Mater. Chem. A* **2014**, *2*, 3317.
[55] H. Guo, Q. Feng, K. Xu, J. Xu, J. Zhu, C. Zhang, T. Liu, *Adv. Funct. Mater.* **2019**, *29*, 1903660.
[56] C. Krishnaraj, H. S. Jena, K. Leus, P. Van Der Voort, *Green Chem.* **2020**, *22*, 1038.
[57] S. Chen, Y. Zheng, B. Zhang, Y. Feng, J. Zhu, J. Xu, C. Zhang, W. Feng, T. Liu, *ACS Appl. Mater. Interfaces* **2019**, *11*, 1384.
[58] B. Volosskiy, H. Fei, Z. Zhao, S. Lee, M. Li, Z. Lin, B. Papandrea, C. Wang, Y. Huang, X. Duan, *ACS Appl. Mater. Interfaces* **2016**, *8*, 26769.
[59] Q. Liu, Y. Wang, L. Dai, J. Yao, *Adv. Mater.* **2016**, *28*, 3000.
[60] J. Zhu, M. Xiao, P. Song, J. Fu, Z. Jin, L. Ma, J. Ge, C. Liu, Z. Chen, W. Xing, *Nano Energy* **2018**, *49*, 23.